Colloids and Surfaces A: Physicochemical and Engineering Aspects 735 (2026) 139499

Contents lists available at ScienceDirect

Colloids and Surfaces A: Physicochemical and Engineering Aspects

journal homepage: www.elsevier.com/locate/colsurfa

Influence of composition and drying method of cellulose/bentonite/CTAB composite on the BPA removal

Mário A.B.S. Nunes [a], Orlando J. Rojas [b,c,d], Denise F.S. Petri [a,*]

[a] Institute of Chemistry, University of São Paulo, Av. Prof. Lineu Prestes 748, São Paulo 05508-000, Brazil
[b] Bioproducts Institute, Department of Chemical and Biological Engineering, The University of British Columbia, 2360 East Mall, Vancouver, BC V6T 1Z3, Canada
[c] Department of Chemistry, The University of British Columbia, 2036 Main Mall, Vancouver, BC V6T 1Z1, Canada
[d] Department of Wood Science, The University of British Columbia, 2424 Main Mall #2900, Vancouver, BC V6T 1Z4, Canada

GRAPHICAL ABSTRACT

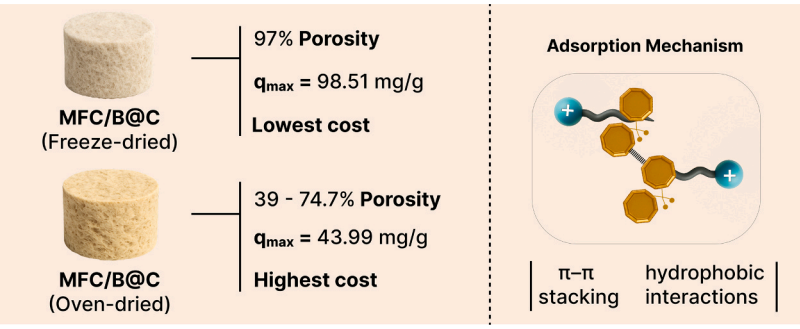

ARTICLE INFO

Keywords:
Cellulose/bentonite composites
CTAB
Bisphenol A
Freeze-drying
Adsorption
Cost/ efficiency analysis

ABSTRACT

Recent studies on cetyltrimethylammonium bromide (CTAB)-modified biopolymers and clay-cellulose composites for organic pollutant removal have focused exclusively on batch adsorption experiments, lacking systematic evaluation of drying method effects on morphological preservation and performance validation in continuous flow systems. This work addresses these critical gaps by investigating microfibrillated cellulose (MFC) composites with CTAB modified bentonite (B@C) for bisphenol A (BPA) removal, systematically comparing freeze-drying versus oven-drying preparation methods. Mercury intrusion porosimetry revealed that freeze-drying preserved three-dimensional porous architecture (porosity ~93 %), whereas oven-drying induced structural collapse (39.2–74.7 % porosity). Batch experiments demonstrated that morphological preservation, rather than total CTAB content, determined adsorptive efficiency; freeze-dried MFC/8B@C achieved q_{max} = 98.51 mg/g versus 43.99 mg/g for oven-dried counterparts, a 159 % improvement despite similar CTAB loading. Fixed-bed column validation, the first reported for CTAB-modified cellulose systems, demonstrated q_o = 115.92 mg/g, surpassing literature values by up to two orders of magnitude. Performance evaluation in freshwater versus ultrapure water revealed natural organic matter interference effects (q_{max} = 74.37 mg/g versus 98.51 mg/g), establishing practical applicability limits absent in previous studies. Integrated economic analysis identified MFC/2B@C as achieving optimal cost-effectiveness ($0.25/L) despite lower adsorption capacity, providing essential guidance for large-scale implementation.

* Corresponding author.
E-mail addresses: mariobsnunes@iq.usp.br (M.A.B.S. Nunes), orlando.rojas@ubc.ca (O.J. Rojas), dfsp@iq.usp.br (D.F.S. Petri).

https://doi.org/10.1016/j.colsurfa.2026.139499
Received 8 October 2025; Received in revised form 9 December 2025; Accepted 5 January 2026
Available online 6 January 2026

1. Introduction

Environmental contamination by bisphenol A (BPA) represents a growing global concern due to its associated risks to human health and aquatic ecosystems [1]. This phenolic compound is extensively utilized in the production of polycarbonates and epoxy resins. BPA acts as an endocrine disruptor capable of interfering with the hormonal system, affecting development, growth, and reproduction in living organisms [2]. Its presence has been detected in diverse water bodies, from industrial effluents to potable water. This widespread contamination necessitates the development of environmentally sustainable and economically viable remediation technologies [3].

Among various technological approaches for treating BPA-contaminated aqueous media—including advanced oxidation processes, biodegradation, and membrane filtration—adsorption stands out for its operational simplicity, low cost, and high efficiency [4]. Adsorbent materials such as activated carbons, zeolites, clay minerals (bentonite), and biologically-based compounds (chitosan) have demonstrated differentiated adsorption capacities [5]. Their efficiencies vary significantly based on specific structural and chemical properties, including specific surface area, porous structure, and functional groups present [6].

Surface modification of adsorbents with cetyltrimethylammonium bromide (CTAB) has emerged as a highly effective strategy to enhance affinity for hydrophobic organic pollutants, such as BPA [7–11]. Studies demonstrated remarkable adsorption capacities, such as 208.3 mg/g for Fe_3O_4@SiO_2/CTAB-SiO_2 composite [7], significantly superior to unmodified materials. This enhancement results primarily from hydrophobic interactions between CTAB alkyl chains and the hydrophobic portion of BPA, complemented by electrostatic and ion dipole interactions [9,12,13].

Microfibrillated cellulose (MFC) and bentonite constitute a promising synergistic combination for developing adsorbent composites. MFC, a renewable and biodegradable biopolymer, offers elevated surface area and excellent mechanical properties, forming three-dimensional porous networks ideal for adsorptive applications [14]. Bentonite, an abundant clay mineral with high cationic exchange capacity [15], when modified with CTAB, provides hydrophobic domains for interaction with apolar organic molecules such as BPA [9]. In this composite matrix, MFC acts as a structural skeleton conferring mouldability, mechanical stability and morphological integrity. Modified bentonite offers specific adsorptive functionality through hydrophobic active sites homogeneously distributed throughout the three-dimensional structure. Analogous strategies employing CTAB modification for BPA removal have been successfully demonstrated in other systems, such as carboxymethylcellulose and sugarcane bagasse cryogels [13].

The drying method in adsorbent preparation influences porous structure, surface area, and morphology [16]. Lyophilization preserves porosity through sublimation of frozen solvent, yielding high-porosity cryogels, while oven drying causes structural collapse via capillary stresses during evaporation, producing denser xerogels [17]. Although established for some cellulosic materials, no studies have systematically compared cryogels and xerogels of the MFC/Bentonite/CTAB system for BPA removal. Recent literature on CTAB-modified biopolymers and clay-cellulose composites for organic pollutant removal presents limitations this work addresses. Existing studies evaluated exclusively batch adsorption without fixed-bed column validation, lacked comparative analysis of drying method effects on morphological properties despite using advanced porosity characterization, and provided insufficient testing in real water matrices [18–22]. While economic considerations appeared in isolated studies, comprehensive cost-benefit optimization balancing adsorption capacity and CTAB content remained absent.

The present investigation aims to comparatively examine the effects of lyophilization versus oven drying on structural properties and adsorptive performance of MFC/bentonite/CTAB composites. Specific objectives include: (i) synthesizing adsorbent composites utilizing both drying methods; (ii) extensively characterizing the physicochemical, morphological, and textural properties of obtained materials; (iii) evaluating BPA adsorption capacity; (iv) correlating observed structural differences with adsorptive performance, and (v) a comparative cost/efficiency analysis.

2. Experimental

2.1. Materials

Cetyltrimethylammonium bromide (CTAB, Sigma Aldrich H5882, 364.45 g/mol, 99 %) and bisphenol A (BPA, Sigma Aldrich 80–05–7, 228.29 $g.mol^{-1}$, 99 %) were used as received. Sodium bentonite was provided by Minature (Gujarat, India). Cellulose fibers extracted from Eucalyptus were donated by the Faculty of Forestry located at the University of British Columbia, Canada.

2.2. Preparation of organo-bentonite

For the synthesis of bentonite/CTAB particles, 10 g of sodium bentonite were added to 200 mL of MilliQ®. The dispersion was added to 200 mL of CTAB at 45×10^{-3} mol/L; the mixture was mechanical stirred at 800 rpm and 80 °C (oil bath) for 5 h. After this step, the clay slurry was vacuum filtered and washed extensively with water to remove the excess of CTAB. The resulting material, a clay paste coded as B@C, had a 67 % moisture content as determined by a Halogen Moisture Analyzer HC103. This procedure was adapted from reference [23]. Pure bentonite and B@C were characterized using XRD analysis, the XRD patterns were recorded on a PANalytical EMPYREAN diffractometer using CuKα radiation (λ = 1.5406 Å) at 45 kV/40 mA. Data were collected from 5 to 90° 2θ in Bragg-Brentano geometry with a PIXcel3D detector and 96.4 s counting time per step. XRD patterns (Supplementary Material **SM1**) obtained for bentonite and B@C indicated the intercalation of CTAB in the bentonite because the interplanar distance increased from 1.3 nm to 1.74 nm. Elemental analysis indicated 1.22 ± 0.04 % N in B@C, which corresponds to 31.7 wt% of CTAB incorporated to B@C. Thermogravimetric analyses (TGA) reported in the literature demonstrated that CTAB incorporation in bentonite ranged between 11.9 wt% [24] and 14.65 wt% [25]. Supplementary Material **SM2** shows SEM images of pure bentonite and B@C.

2.3. Preparation and characterization of the MFC/B@C xerogels and cryogels

Fig. 1 shows the steps to produce xerogels and cryogels. First, dried cellulose fibers were ground in a blender (Black+Decker BL2010BG). Following this stage, wet pulp production was conducted using a mechanical stirrer (IKA Eurostar 60) at 1000 rpm for approximately 1 h. Vacuum filtration was performed, and moisture content was measured at 87 % using the Halogen Moisture Analyzer HC103. In the following step, a mixture was prepared by dispersing 2 g or 8 g of B@C paste (67 % moisture) and 37.5 g of microfibrillated cellulose (MFC) pulp (87 % moisture) in 50 mL of MilliQ® water, followed by manual stirring with a glass rod for 15 min, the corresponding compositions were coded as MFC/2B@C or MFC/8B@C, respectively. Subsequently, the systems were added to silicone molds (Supplementary Material **SM3**) and dried by two distinct methods. Xerogels were dried in oven at 100 °C for 48 h, whereas cryogels were obtained after 24 h freeze-drying (Terroni LT600, Brazil). The xerogels were coded as $MFC^{O.}$, $MFC/2B@C^{O.}$, and $MFC/8B@C^{O.}$. The cryogels were coded as $MFC^{F.D.}$, $MFC/2B@C^{F.D.}$, and $MFC/8B@C^{F.D.}$. Table 1 shows their compositions. Supplementary Material **SM4** shows the digital photographs of the dried composites and pure MFC.

Dry MFC, B@C, $MFC/2B@C^{O.}$, $MFC/8B@C^{O.}$, $MFC/2B@C^{F.D.}$, and $MFC/8B@C^{F.D.}$ were characterized by elemental analyses (CHN) using a

Perkin Elmer 2400 series ii elemental analyzer. FTIR-ATR spectra were acquired in an Alpha FTIR equipment (Bruker, Germany) using a ZuSe crystal with accumulation of 64 scans, at resolution of 4 cm^{-1} and in the spectral range of 400–4000 cm^{-1}. Scanning electron microscopy (SEM) analyses were performed for gold-sputtered samples in a SEM Jeol 6460 LV microscope operating at a voltage of 15 kV. Swelling degree and surface tension analysis were obtained in a Krüss K100 (Krüss GmbH, Germany) tensiometer. Point of zero charge measurements were obtained using a Digimed DM-22 pHmeter. Mercury intrusion porosimetry (AutoPore IV – Micromeritics) was used to determine the porosity and pore size distribution, according to the procedure described by ISO 15901–1/2005 standard.

2.4. Batch adsorption studies

Stock solution of BPA at 276 mg/L was prepared by dissolving BPA (Sigma-Aldrich, 228.31 g/mol) in MilliQ® water or fresh water from a dam located inside the University of São Paulo. The fresh water presented pH 6.34 and conductivity of 81.5 μS/cm. The UV-Vis spectrum of fresh water (Supplementary Material **SM5)** showed absorbance higher than 0.2 in the spectral range of 200 nm to 240 nm, indicating the possible presence of nitrate and carbonate ions, and organic molecules (humic and fulvic acids). To dissolve BPA, the water was heated at 80 °C and BPA was added gradually under magnetic stirring until complete dissolution.

The adsorption kinetic experiments were performed for BPA (10 mL) at pH 6.12, at an initial concentration (C_0) of 120 mg/L, using MFC/2B@$C^{O.}$, MFC/8B@$C^{O.}$, MFC/2B@$C^{F.D.}$, and MFC/8B@$C^{F.D.}$. The mass of adsorbent was ~ 10 mg. Notably, BPA did not adsorb onto pure MFC nor on MFC/B (microfibrillated cellulose with unmodified bentonite). The experiments were conducted under continuous shaking at (22 ± 1) °C with contact time of 1, 3, 5, 10, 15, 20, 30, 40, 50, and 60 min. The concentration of BPA remaining in the supernatant (C_e) was determined by measuring the absorbance at 275 nm, which corresponds to the wavelength of maximum absorption of BPA, using a Beckman-Coulter DU650 spectrophotometer. Supplementary Material **SM6** shows the calibration curve for BPA at 275 nm.

The adsorption isotherms of BPA on MFC/2B@$C^{O.}$, MFC/8B@$C^{O.}$, MFC/2B@$C^{F.D.}$, and MFC/8B@$C^{F.D.}$ adsorbents were performed at (22 ± 1) °C. A fixed amount of adsorbent (m) of 10 mg was added to 10 mL of BPA (pH 6.12) solutions, in the concentration range from 20 mg/L to 276 mg/L. The vials were kept under shaking for 60 min. All experiments were repeated at least twice. The equilibrium adsorption capacity (q_e, mg/g) was calculated using Eq. (1).

$$q_e = \frac{C_0 - C_e}{m} \times V \quad (1)$$

where V is the solution volume.

The adsorption performance (removal efficiency and equilibrium adsorption capacity) of MFC/2B@$C^{O.}$, MFC/8B@$C^{O.}$, MFC/2B@$C^{F.D.}$, and MFC/8B@$C^{F.D.}$ adsorbents (10 mg) was also investigated under dilute condition. Batch experiments were carried out at (22 ± 1) °C, using BPA at 1.0 mg/L, V = 10 mL, pH 6.10, in the absence and in the presence of competing ions (Mg^{2+}, Ca^{2+}, Na^{+}, and K^{+} ions), with each ion present at a concentration of 10 mg L^{-1}), which is comparable to levels found in natural waters. Unfortunately, BPA concentrations below 0.1 mg/L could not be tested due to the insufficient detection limit of UV spectrophotometry.

Table 1
Nomenclature of the evaluated compositions with percentage of each component. The contents of CTAB incorporated in bentonite (in parentheses) were determined using CHN.

Compositions	Drying Method	B@C (wt%)	MFC (wt%)
MFC/2B@$C^{O.}$	Oven	12 (8.9 wt% CTAB)	88
MFC/2B@$C^{F.D.}$	Freeze-drying	12 (8.9 wt% CTAB)	
MFC/8B@$C^{O.}$	Oven	35.2 (16.7 wt% CTAB)	64.8
MFC/8B@$C^{F.D.}$	Freeze-drying	35.2 (18.5 wt% CTAB)	

2.5. Column adsorption studies

Column adsorption experiments were conducted using polyethylene columns of 14 mm diameter and 10 cm long, coupled to silicone Tygon® tubes attached to a peristaltic pump, at 22 °C, and the effluent were taken at regular interval in the removal process (Supplementary Material **SM7**). To optimize the operational parameters, the drying method,

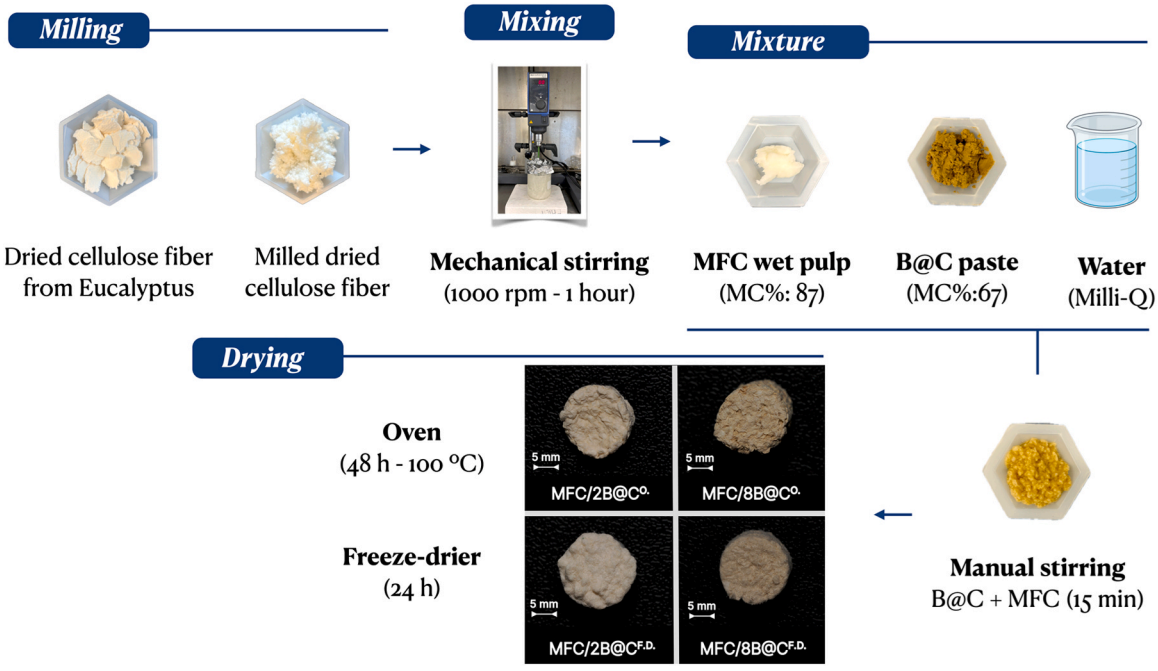

Fig. 1. Experimental methodology to produce MFC/B@C xerogels and cryogels.

composition, and the medium (distilled water and fresh water) were varied. The initial concentration (C_0) of BPA (276 mg/L or 291 mg/L) and the flow rate ($\nu = 0.4$ mL/min) were kept constant in all the experiments. The BPA solutions in MilliQ® water and fresh water had pH of 6.12 and 7, respectively. UV spectrophotometer (Beckman-Coulter DU650) was employed to measure the concentration of BPA at 275 nm. The eluents that came out of the column were analyzed by UV-Vis after subtracting the blank run with the MilliQ® water or fresh water.

3. Results and discussion

3.1. Characterization of the MFC/B@C xerogels and cryogels

The elemental analysis revealed that the nitrogen content directly correlated with initial incorporation of B@C to the MFC systems. Both MFC/2B@$C^{O.}$ and MFC/2B@$C^{F.D.}$ presented (0.34 ± 0.10) % N, which corresponds to 8.9 wt% of CTAB in the composites. MFC/8B@$C^{O.}$ and MFC/8B@$C^{F.D.}$ compositions presented (0.63 ± 0.01) % N (16.7 wt% CTAB) and (0.71 ± 0.01) % N (18.5 wt% CTAB), respectively (Table 1 and Supplementary Material **SM8**). Therefore, the drying method had no significant impact on the amount of B@C incorporated to the composites.

Supplementary Material **SM8** presents SEM images of MFC, MFC/2B@$C^{O.}$, MFC/8B@$C^{O.}$, MFC/2B@$C^{F.D.}$, and MFC/8B@$C^{F.D.}$ before the adsorption. MFC presented typical morphology of cellulose microfibrils. Following B@C incorporation, the fibers appeared coated with particles. MFC/2B@C demonstrated uniform distribution of B@C particles, whereas MFC/8B@C exhibited pronounced agglomeration. Similar clustering behavior has been observed in chitosan-halloysite xerogels at 3 wt% concentration [26]. Freeze-drying significantly improved the adhesion of B@C particles to the fibers, as the process preserved the porous and entangled structure of the fiber network. In contrast, oven-drying caused fiber shrinkage and rearrangement, leaving more free space among the fibers and reducing the available contact area for particle attachment. Fig. 2 shows SEM images of MFC/8B@$C^{O.}$ xerogel, and MFC/8B@$C^{F.D.}$ cryogel before and after the adsorption process. Post-adsorption morphological examination confirmed structural integrity, with B@C particles maintaining strong adhesion to fiber surfaces, demonstrating excellent composite stability.

Fig. 3 demonstrates that both drying method and B@C content significantly influenced composite density. Without B@C incorporation, MFC cryogels and xerogels exhibited densities of 0.103 g/cm³ and 0.151 g/cm³ , respectively. B@C addition increased xerogel densities substantially: MFC/2B@$C^{O.}$ and MFC/8B@$C^{O.}$ xerogels reached 0.185 g/cm³ and 0.384 g/cm³ , respectively. Conversely, MFC/2B@$C^{F.D.}$ and MFC/8B@$C^{F.D.}$ cryogels maintained considerably lower densities of 0.086 g/cm³ and 0.165 g/cm³ . These findings align with established literature patterns for cellulose-based composites. Previous study [17] reported cellulose aerogels achieving densities of 0.054–0.215 g/cm³ depending on cellulose concentration in the initial solution (3–11 wt%), while cellulose cryogels demonstrate values as low as 0.050 g/cm³ with 97 % porosity. Cellulose xerogels consistently exhibit higher densities (0.290–0.491 g/cm³) due to solvent drying effects, with the variation attributed to different solvents used (isopropanol vs ethanol) [17].

Fig. 3 shows the porosity, surface area, and mean pore diameter determined for all xerogels and cryogels using mercury intrusion porosimeter measurements. The highest porosity and surface area values were obtained for the cryogels, reaching values as high as 93.7 % and 51.87 m²/g. Cryogels of MFC presented surface area of 37.50 m²/g and porosity of 92.6 %, which are similar to those reported by Buchtova et al. [27], and much higher than those observed for MFC xerogels (0.57 m²/g and 72.4 % porosity). A similar trend was observed for alginate beads; air dried beads presented porosity of 20 ± 2 %, whereas freeze-dried beads showed 77 ± 3 % of porosity [28].

The content of B@C in the composites affected the microstructural characteristics. MFC/2B@$C^{O.}$ presented the lowest surface area (0.23 m²/g) and porosity (39.2 %) values, indicating structural collapse with material densification. Nevertheless, MFC/8B@$C^{O.}$ displayed surface area of 18.18 m²/g and porosity of 74.7 %. This suggests that the increase in B@C fraction (from 12 wt% to 35.2 wt%) contributed more significantly to the composite's total surface area increment. Similar composition-dependent effects occurred in chitosan-clay cryogel systems, where varying kaolin-MAPTES content produced substantial changes in textural parameters [29]. For instance, increasing clay content from P1-K to P3-K resulted in surface area ranging from 1.812 to 3.067 m²/g, while pore volume increased from 0.005 to 0.013 cm³ /g. The most significant effects were observed in the chitosan-based series. P9-K achieved surface area of 8.322 m²/g and pore volume of 0.023 cm³ /g, showing that both clay concentration and chitosan type synergistically influence final textural properties. [29]. The xerogels presented mean pore diameter varying from 24 μm to 47 μm.

For the cryogels, B@C particles provided a progressive increase in surface area from 37.50 m²/g to 44.73 m²/g (MFC/2B@$C^{F.D.}$) and 51.87 m²/g (MFC/8B@$C^{F.D.}$), while preserving high porosity (~ 93 %). Noteworthy, the high porosity arises primarily from the MFC network, not from bentonite particles. The average pore diameter remained relatively constant (30–33 μm), regardless of composition, indicating

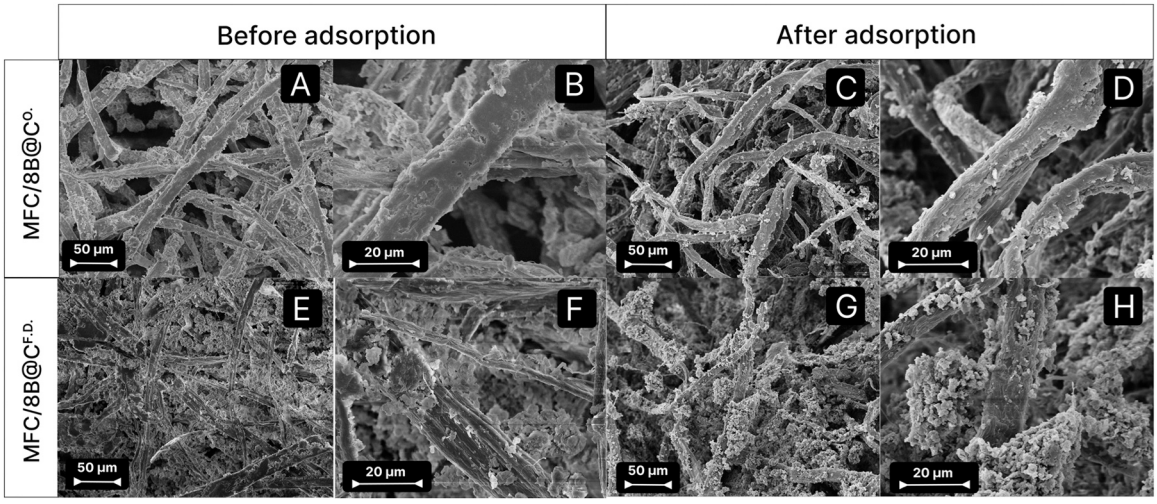

Fig. 2. Scanning electron microscopy images obtained for MFC/8B@$C^{O.}$xerogel before (A, B) and after the adsorption process (C, D), and MFC/8B@$C^{F.D.}$cryogel before (E, F) and after the adsorption process (G, H).

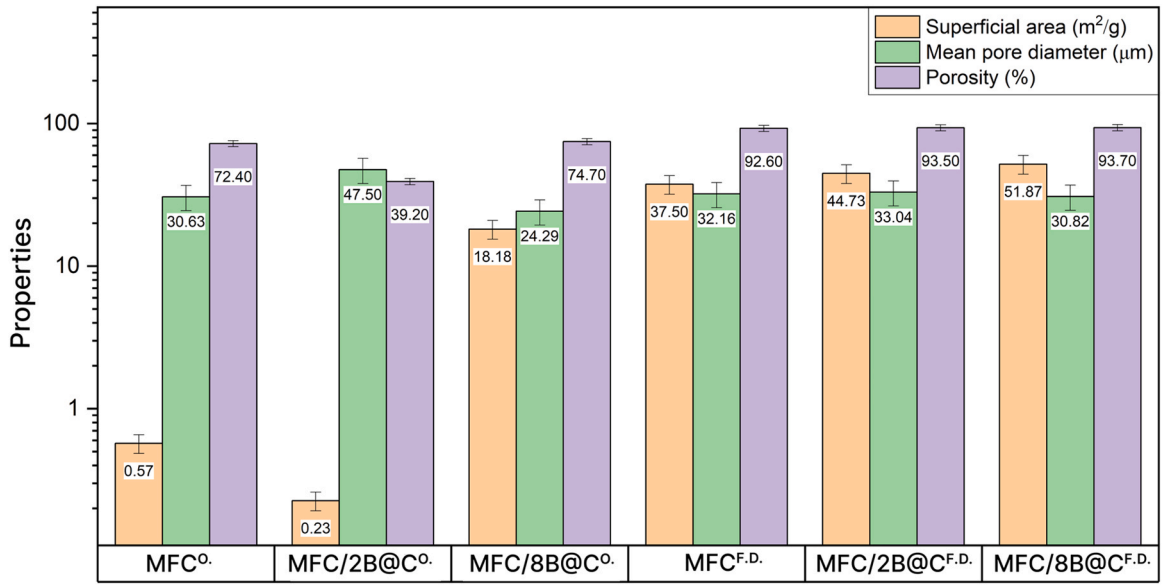

Fig. 3. Surface area, average pore diameter, porosity and density obtained from mercury intrusion porosimetry for MFC$^{O.}$, MFC/2B@C$^{O.}$, and MFC/8B@C$^{O.}$ xerogels, and MFC$^{F.D.}$, MFC/2B@C$^{F.D.}$, and MFC/8B@C$^{F.D.}$ cryogels.

preservation of the porous macrostructure during ice crystals sublimation. This preservation aligns with findings from supercritical CO_2 processing studies, where aerogels with exfoliated clay maintained superior structural integrity compared to those with intercalated clay. Specifically, s-PS aerogels with 20 wt% exfoliated OMMT achieved surface areas of 281 m^2/g compared to only 166 m^2/g for intercalated clay aerogels, demonstrating that clay particle state critically influenced textural preservation during processing [30]. The density values correlated well with the porosity values. The cryogels presented the highest porosity and the lowest density values. This trend was also observed for cellulose-graphene oxide cryogels with 98.62 % porosity and extremely low densities of 0.0154 g/cm^3 [31].

The determination of point of zero charge (PZC) of adsorbents is important to understand the adsorption behavior under different pH values. Supplementary Material **SM9** shows the determination of PZC for pure bentonite, B@C, MFC/2B@C$^{O.}$, MFC/8B@C$^{O.}$, MFC/2B@C$^{F.D.}$, and MFC/8B@C$^{F.D.}$. The silica groups in bentonite render a net negative charge at in the pH range of 2.0–9.0 [32]. However, B@C and the composites exhibited PZC values ranging from 5.8 to 6.4 due to Na-montmorillonite edges that contain Si–OH, Al–OH, and Mg–OH groups and to the quaternary ammonium groups [33]. CTAB exhibits PZC at pH ~ 4, while BPA presents pKa values between 9.6 and 10.2, establishing the fundamental charge behavior parameters for the system [34,35]. The adsorption experiments of BPA were carried out in MilliQ water (pH 6.12) or fresh water (pH 7); under these pH conditions the adsorption is expected to be mainly driven by hydrophobic interactions rather than electrostatic interactions because both adsorbent and adsorbate are weakly charged [7]

Fig. 4 shows that freeze-dried samples presented a higher swelling capacity compared to oven-dried samples (843.2 % versus 600.9 % for MFC/2B@C and 693.8 % versus 448.2 % for MFC/8B@C). Cryogels presented superior porosity (~ 93 %) compared to xerogels (39.2 % for MFC/2B@C and 74.7 % for MFC/8B@C), as shown in Fig. 3. Therefore, this phenomenon was attributed to the preservation of porous structure during freeze-drying that facilitated water penetration.

The xerogels were dried at 100 °C for 48 h, these conditions might induce "hornification" of cellulose chains/fibrils. Briefly, the "hornification" results from local ordering driven by intermolecular H bonding that resist upon rewetting. During oven drying process, water molecules are removed by evaporation, enabling the formation of hydrogen-bonded networks with different sizes and dispersive forces

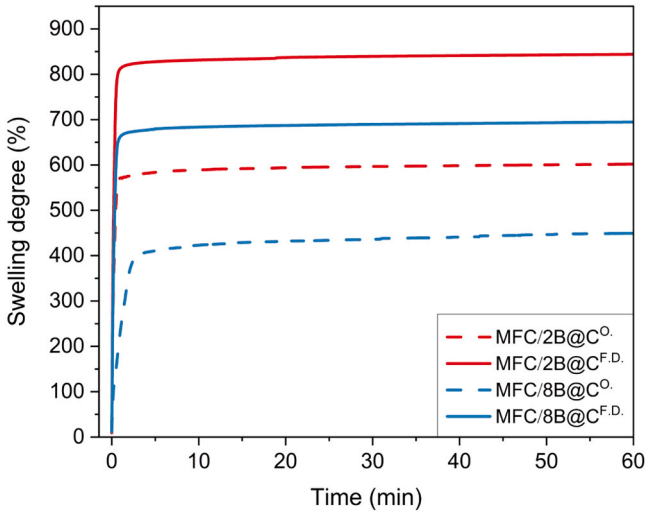

Fig. 4. Degree of swelling (%) for MFC, MFC/2B@C$^{O.}$, and MFC/8B@C $^{O.}$ xerogels, and MFC/2B@C$^{F.D.}$ and MFC/8B@C $^{F.D.}$ cryogels samples in MilliQ® water, at (22 ± 1) °C.

might contribute to the cohesion among the fibers [36].

The increase of B@C content in the composites reduced the swelling degree in approximately 150 %. B@C particles exhibit predominantly hydrophobic character due to CTAB modification, whose hydrocarbon chains convert the bentonite surface to organophilic, consequently reducing water affinity and limiting swelling [37]. The MFC/2B@C composition contains 23.2 wt% more microfibrillated cellulose (hydrophilic) compared to the MFC/8B@C composition.

Fourier-transform infrared spectroscopy (FTIR) was used to investigate the structural changes in natural bentonite before and after intercalation with CTAB, as well as in cellulose xerogels and cryogels with different B@C contents, as presented in Fig. 5. The spectrum of bentonite showed a characteristic set of absorption bands: The O–H stretching vibration at 3407 cm^{-1} was attributed to surface and interlayer water, while the stretching vibration of the silanol group (Si–OH) was observed at 3619 cm^{-1} . The band at 1634 cm^{-1} corresponded to the H–O–H bending vibrations of adsorbed water molecules. The

characteristic vibrations of the Si–O–Al, Si–O–Si, and Si–O groups from the tetrahedral layer appeared at 1111 cm^{-1} and 998 cm^{-1} . Additionally, bands at 796 cm^{-1} , 523 cm^{-1} , and 461 cm^{-1} were associated with further stretching and bending vibrations of Si–O and Si–O–Si [38].

Intercalation with CTAB led to the appearance of new absorption bands at 2918 cm^{-1} and 2849 cm^{-1} , attributed to the asymmetric and symmetric stretching vibrations of methylene (–CH_2) and methyl (–CH) groups present in the alkyl chains of the surfactant [39]. Moreover, the band at 1468 cm^{-1} , corresponding to the bending vibrations of the quaternary ammonium group (NH_4^+), confirmed the successful intercalation of CTAB molecules between the silica layers of the bentonite [40].

For MFC, the O–H stretching vibrations from hydroxy groups were observed at 3331 cm^{-1} , while the CH_2 bending vibrations appeared at 1428 cm^{-1} . In-plane CH and OH bending vibrations were detected at 1365 cm^{-1} and 1315 cm^{-1} , respectively. The band at 1161 cm^{-1} was attributed to the C–O–C stretching vibration of glycosidic linkages, while the C–O stretching vibrations associated with primary and secondary alcohol groups were observed at 1105 cm^{-1} and 1053 cm^{-1} . The combined C–H and C–OH stretching vibration was seen at 1030 cm^{-1} , and the β-glycosidic linkages between glucose units were identified by the band at 896 cm^{-1} . Finally, the bands at 661 cm^{-1} , 608 cm^{-1} , 558 cm^{-1} , and 437 cm^{-1} were related to vibrations associated with the crystalline structure of cellulose [41].

FTIR analysis of MFC/B@C composites confirmed characteristic CTAB bands: –CH_2 and –CH stretching at 2918–2919 and 2848–2851 cm^{-1} , –CH_2/–CH_3 bending at 1469 cm^{-1} , trimethylammonium deformation at 1370 cm^{-1} , and C-N vibrations at 1158–1108 cm^{-1} [42,43]. Spectral comparison shows minimal positional shifts (< 3 cm^{-1}) between xerogels and cryogels at equivalent B@C contents, but intensity variations directly correlated with surfactant content since MFC/8B@C exhibited stronger CTAB bands than MFC/2B@C. The consistent presence of these diagnostic bands, particularly the 1469 cm^{-1} marker, across all composites regardless of drying method confirms effective CTAB intercalation.

The molecular mechanism of BPA adsorption can be better supported by DFT calculations performed for the BPA-CTAB system [12]. The most stable geometry revealed three interaction types: ion-dipole between bromide and BPA hydroxyl (2.23 Å), hydrogen bonding between BPA hydroxyl and CTAB methylene (2.77 Å), and electrostatic interaction between quaternary ammonium and bromide (3.90 Å), with a complexation energy of −27.40 kcal/mol [12]. The high efficiency of CTAB stems from strong bromide association (77 %) with positively charged micelle surfaces, attributed to their large size and polarizability [44].

3.2. The effect of drying method and composition on the adsorption behavior

3.2.1. Adsorption kinetic studies

Fig. 6 shows the adsorption kinetic curves of BPA (C_0 = 276 mg/L) on MFC/2B@$C^{O.}$, MFC/8B@$C^{O.}$, MFC/2B@$C^{F.D}$., and MFC/8B@$C^{F.D.}$ at 22 ± 1 °C and pH 6.12, using 10 mg of adsorbent mass and 10 mL of BPA solution. The experimental data fitted well to the intraparticle diffusion, Elovich models (provided in the Supplementary Material **SM10**) and pseudo-second order models (Fig. 6 and Table 2). Regardless of the composite type, the adsorption equilibrium was achieved after one hour of adsorption. However, in the case of MFC/8B@$C^{F.D.}$ the q_e values in the plateau region have been achieved in the shortest time of 30 min. One should notice that BPA did not adsorb on MFC$^{O.}$, MFC$^{F.D.}$, or pure bentonite even after 24 h contact.

The adsorption kinetics of BPA on freeze-dried compositions demonstrated superior performance compared to established CTAB-

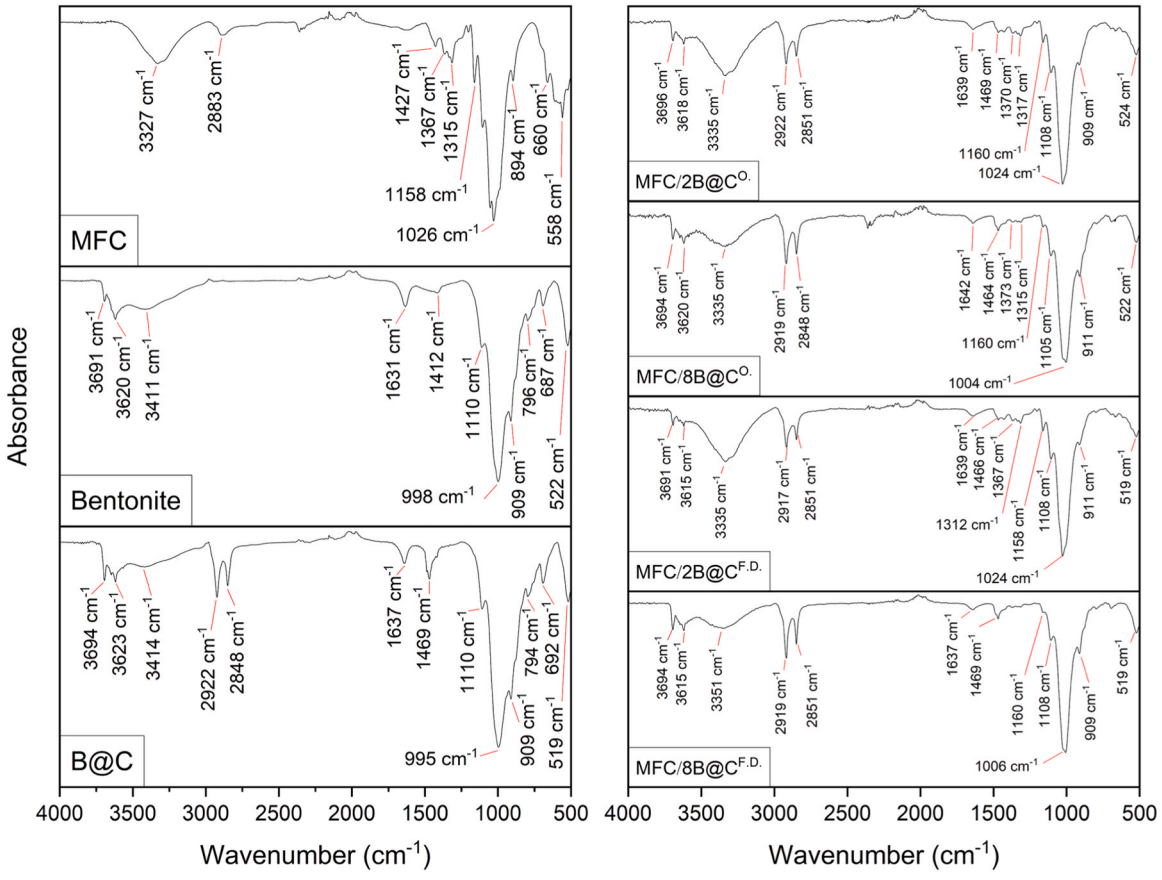

Fig. 5. FTIR spectra of pristine MFC, pure bentonite, B@C, MFC/2B@$C^{O.}$, and MFC/8B@$C^{O.}$ xerogels, and MFC/2B@$C^{F.D.}$ and MFC/8B@$C^{F.D.}$ cryogels.

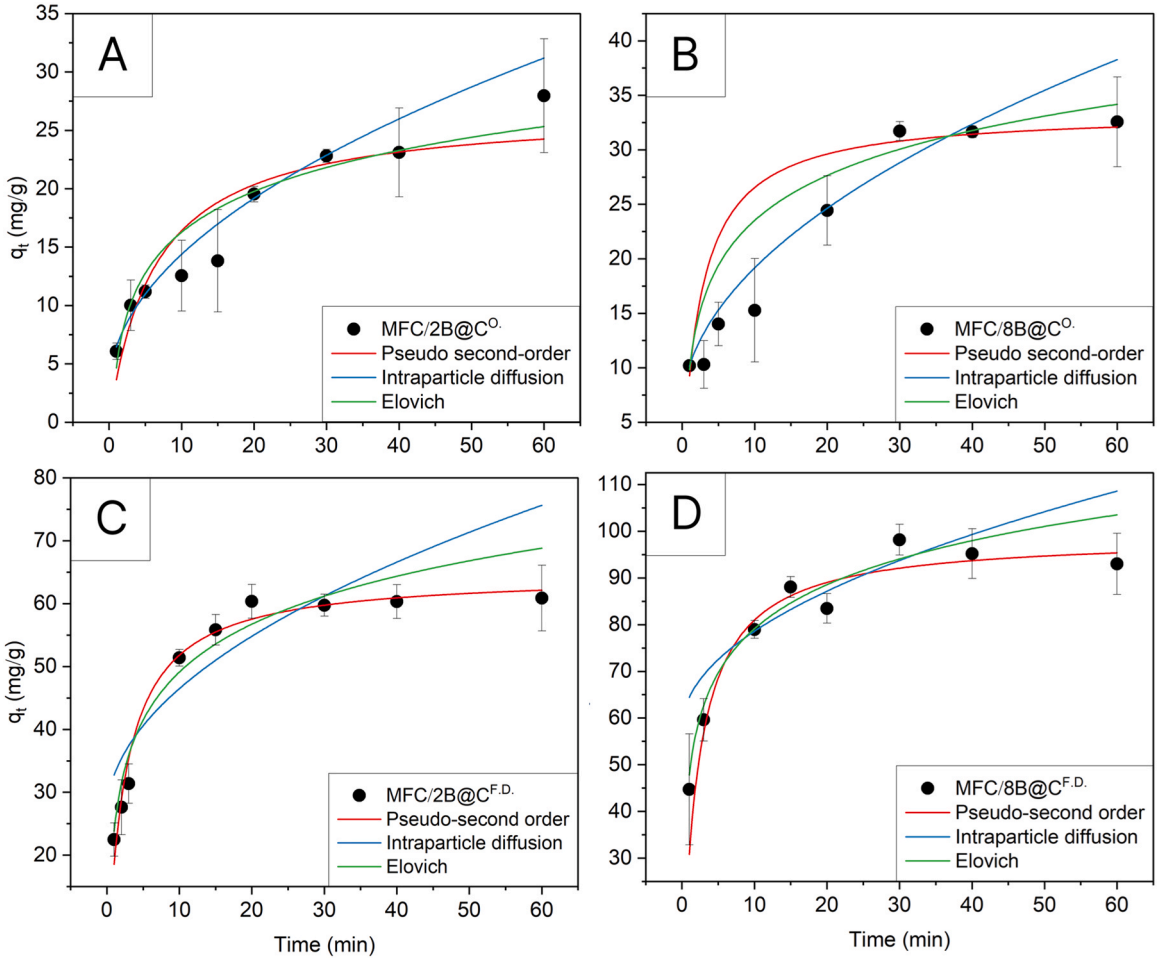

Fig. 6. Adsorption kinetic curves for (A) MFC/2B@C$^{O.}$, (B) MFC/8B@C$^{O.}$, (C) MFC/2B@C$^{F.D.}$., and (D) MFC/8B@C$^{F.D.}$, at 22 ± 1 °C and pH 6.12, adsorbent mass (m) = 10 mg, and V = 10 mL. The lines are the nonlinear fittings to the intraparticle diffusion model, Elovich, and pseudo-second order model, respectively.

Table 2
Adsorption kinetic parameters for BPA on different adsorbents fitted to pseudo-second-order model.

Pseudo-second order				
Adsorbent	k_2 [g/(mg·min)]	q_e (mg/g)	R^2	REF
Fe_3O_4@SiO_2/CTAB-SiO_2	0.006	93.4	0.999	[7]
2.0 CEC-C_{16} DI	0.06	19.57	0.9999	[10]
2.0 CEC-C_{16} -AH	0.15	19.96	1.000	[10]
γAlNPs-CTAB	0.0673	13.959	0.991	[45]
CTAB-Ms(x)	0.0012	85.58	0.9998	[46]
CTAB-Mullite	0.869	0.050	0.97	[8]
MFC/2B@C$^{O.}$	0.005857	26.82	0.990	This work
MFC/8B@C$^{O.}$	0.01146	33.48	0.963	
MFC/2B@C$^{F.D.}$	0.006195	64.71	0.9782	
MFC/8B@C$^{F.D.}$	0.004574	98.87	0.8621	

modified adsorbents. The pseudo-second order model [47], which describes the rate-limiting step in adsorption processes and is expressed as $t/q_t = 1/(k_2 q_e^2) + t/q_e$, where q_t (mg/g) represents the adsorption capacity at time t, q_e (mg/g) is the equilibrium adsorption capacity, and k_2 (g/mg·min) denotes the pseudo-second order rate constant. Among the synthesized materials, MFC/8B@C$^{F.D.}$ demonstrated exceptional performance with the highest adsorption capacity (q_e = 98.87 mg/g), while MFC/8B@C$^{O.}$, significantly outperforming the oven drying composition (q_e = 33.48 mg/g). The same trend was observed for MFC/2B@C$^{F.D.}$ (q_e = 64.71 mg/g) and MFC/2B@C$^{O.}$ (q_e = 26.82 mg/g). The freeze-dried composition MFC/8B@C$^{F.D.}$ not only exceeded the performance of conventional dried materials but also significantly surpassed CTAB-functionalized walnut shell (q_e = 22.3–33.4 mg/g) [48] and approached the high capacity of CTAB-modified SiO_2 performance (q_e = 85.58 mg/g) [46], demonstrating the effectiveness of the freeze-drying process combined with higher CTAB fractions.

The 2.9-fold capacity improvement of freeze-dried over oven-dried samples (98.87 mg/g *vs* 33.48 mg/g for MFC/8B@C) demonstrated the critical role of processing method. This trend aligns with the highest porosity and surface area values determined for cryogels (Fig. 3). Freeze-drying preserves porous architecture and surface accessibility, maintaining adsorption site integrity that oven-drying compromises [49]. The strong correlations observed for both Elovich ($R^2 > 0.98$) and intraparticle diffusion models ($R^2 > 0.99$) indicate complex mechanisms involving both physisorption and pore diffusion. The intraparticle diffusion model evaluates whether pore diffusion controls the adsorption rate through $q_t = k_i d \cdot t^{(1/2)} + C$, where $k_i d$ (mg/g·min$^{(1/2)}$) represents the intraparticle diffusion rate constant and C provides information about boundary layer thickness. This behavior is consistent with organically modified clay from Burkina Faso [10], where multiple kinetic models were required to comprehensively describe the adsorption process.

3.2.2. *Adsorption isotherms*

Fig. 7 shows the adsorption isotherms for BPA dissolved in MilliQ® water (pH 6.12) and fresh water (pH 7) on MFC/2B@C$^{O.}$, MFC/8B@C$^{O.}$, MFC/2B@C$^{F.D.}$, and MFC/8B@C$^{F.D.}$ adsorbents. All experiments were conducted at 22 ± 1 °C after one hour of contact, using 10 mg of adsorbent and 10 mL of BPA solution.

To evaluate BPA adsorption mechanisms, experimental isotherms were fitted using Langmuir [50], Freundlich [51], Redlich-Peterson [52], and Temkin models [53] (with the calculated parameters showed in the Table 3 and in the Supplementary Material **SM11**, respectively). The Redlich-Peterson model demonstrated exceptional performance across all compositions, consistently yielding superior statistical parameters with R^2 values of approximately 0.995, with parameters revealing distinct adsorption characteristics: MFC/8B@$C^{F.D.}$ exhibited the highest K_R value (11.33 ± 1.7 L/g) and g parameter (0.7538 ± 0.034), while MFC/2B@$C^{O.}$ demonstrated the lowest K_R (1.546 ± 0.48 L/g) and intermediate g value (0.7699 ± 0.098). The g parameter values between 0.67 and 0.85 indicate hybrid adsorption behavior combining favorable heterogeneous surface interactions with partial multilayer formation. Comparatively, established CTAB-modified systems show different Redlich-Peterson characteristics: KF/CTAB presents KRP = 0.0277 L/mg, a_{RP} = 0.650 (L/mg), and β_{RP} = 0.967 [1], while Fe_3O_4@SiO_2/CTAB-SiO_2 exhibits significantly higher K_{RP} = 358.5 L/mg and a_{RP} = 3.83 (L/mg) with β_{RP} = 0.699 [2], demonstrating the diverse adsorption mechanisms achieved through different CTAB modification strategies.

The BPA adsorption isotherms of the freeze-dried adsorbents outperform previously reported CTAB-modified materials: MFC/2B@$C^{F.}$

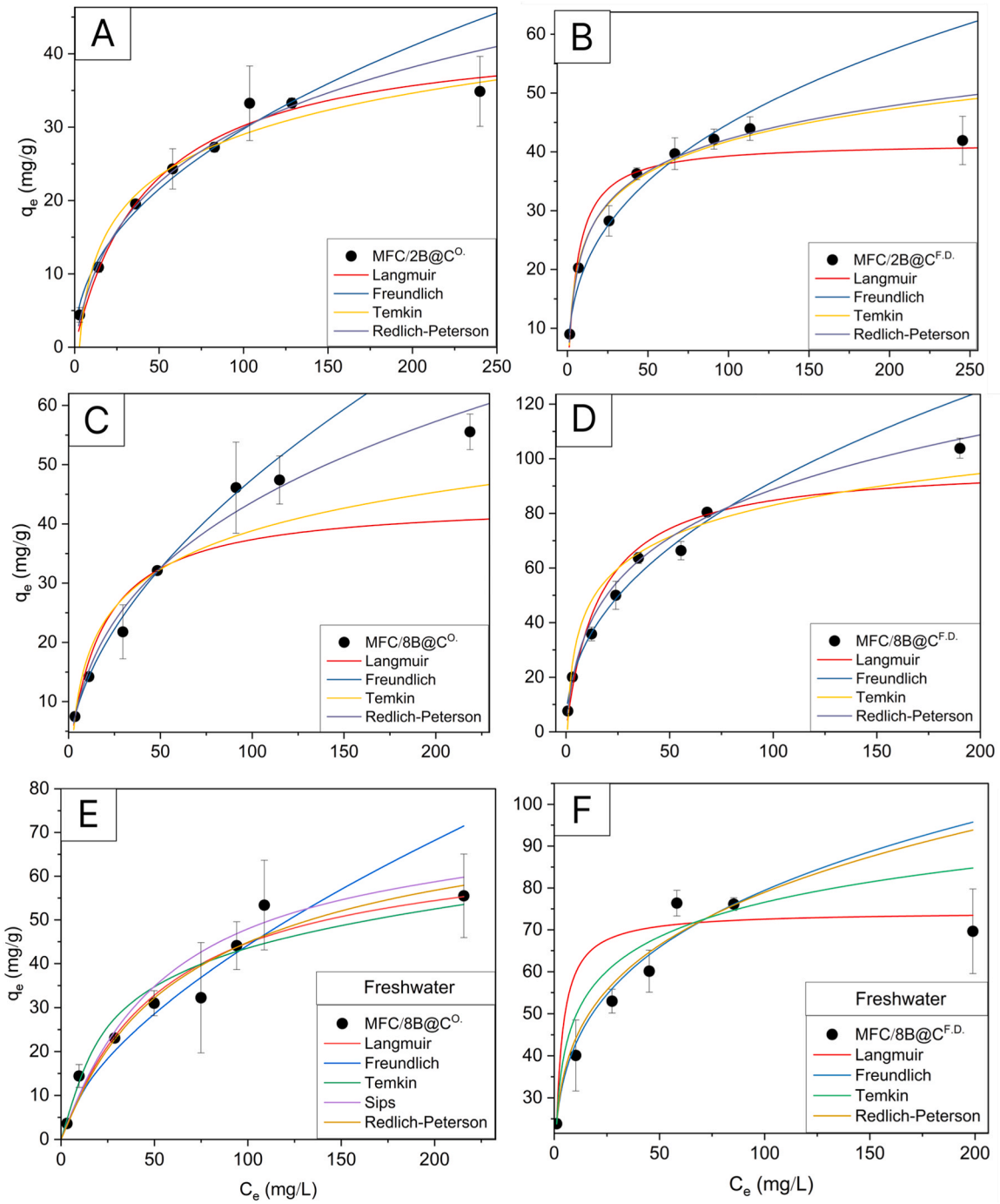

Fig. 7. Adsorption isotherms for BPA dissolved in MilliQ water (pH 6.12) on (A) MFC/2B@$C^{O.}$, (B) MFC/8B@$C^{O.}$, (C) MFC/2B@$C^{F.D.}$, and (D) MFC/8B@$C^{F.D.}$ adsorbents, and for BPA dissolved in fresh water (pH 7) on (E) MFC/8B@$C^{O.}$ and (F) MFC/8B@$C^{F.D.}$. All experiments were conducted at 22 ± 1 °C, one hour contact time, adsorbent mass = 10 mg, and solution volume = 10 mL.

Table 3
Langmuir (q_{max}, K_L) and Redlich-Peterson fitting parameters (K_{RP}, a_{RP}, β_{RP}) determined for the adsorption of BPA onto different adsorbents modified with CTAB.

Langmuir Model				
Adsorbent	q_{max} (mg/g)	K_L (L/mg)	R^2	REF
MFC and MFC/B	0	-	-	This work
MFC/2B@$C^{O.}$	43.53	0.02263	0.9913	
MFC/2B@$C^{F.D.}$	41.61	0.1696	0.9783	
MFC/8B@$C^{O.}$	43.99	0.0563	0.996	
MFC/8B@$C^{F.D.}$	98.51	0.06168	0.9822	
MFC/8B@$C^{O.}$ *	69.89	0.017829	0.9431	
MFC/8B@$C^{F.D.}$ *	74.37	0.3985	0.964	
Fe_3O_4@SiO_2/CTAB-SiO_2	208.3	0.51	0.970	[7]
CTAB-Ms(x)	198.80	0.354	0.948	[46]
MSN-CTAB	128.19	0.2829	0.974	[11]
2.0 CEC-C16-AH	119.1	0.44	0.980	[10]
2.0 CEC-C16-DI	111.1	0.34	0.974	[10]
KF/CTAB	41.66	0.225	0.951	[12]
WNS-CTAB	25.1	0.46	0.940	[48]
γANPs-CTAB	17.4825	0.0403	0.920	[45]
Bentonite/CTAB	15.22	0.16	0.910	[9]
CTAB-Mullite	0.483	0.255	0.997	[8]

Redlich-Peterson model					
Adsorbent	K_{RP} (L/mg)	a_{RP} (L/mg)	β_{RP}	R^2	REF
KF/CTAB	0.0277	0.650	0.967	0.977	[12]
Fe_3O_4@SiO_2/CTAB-SiO_2	358.5	3.83	0.699	0.989	[7]
MFC/2B@$C^{O.}$	1.546	0.1201	0.7699	0.9954	This
MFC/2B@$C^{F.D.}$	10.07	0.4613	0.8477	0.996	work
MFC/8B@$C^{O.}$	3.902	0.3643	0.6691	0.9995	
MFC/2B@$C^{F.D.}$	11.33	0.3653	0.7538	0.9956	

Legend: MFC/8B@$C^{F.D.*}$ and MFC/8B@C $O.*$ = adsorbents tested in freshwater (from the dam).

$^{D.}$ showed an excellent Langmuir fit (q_{max} = 41.61 ± 0.91 mg/g, K_L = 0.1696 ± 0.009 L/mg, R^2 = 0.9783), while MFC/8B@$C^{F.D.}$ achieved superior capacity (q_{max} = 98.51 ± 2.3 mg/g, K_L = 0.06168 ± 0.0051 L/mg, R^2 = 0.9822). This improvement indicates that adsorptive performance scales with textural properties, specifically CTAB-domain accessibility and morphology preservation, rather than total surfactant amount, as evidenced by increased porosity and surface area (Fig. 3). These values surpass other CTAB-modified systems, including KF/CTAB (q_{max} = 41.66 mg/g) [12], WNS-CTAB (q_{max} = 25.1 mg/g) [48], and γANPs-CTAB (q_{max} = 17.48 mg/g) [45]. No measurable BPA uptake was observed on unmodified MFC or MFC/B, indicating that CTAB incorporation is essential to form hydrophobic domains required for BPA interaction (Table 3). The Langmuir constants K_L, which represent the binding affinity between BPA and the adsorbent surface, demonstrate that freeze-drying effects vary with CTAB content: MFC/8B@C shows marginally increased K_L (0.06168 vs 0.05639 L/mg) while MFC/2B@C exhibits significantly enhanced K_L (0.1696 vs 0.02263 L/mg), indicating that structural optimization becomes dominant over binding affinity at higher CTAB loadings.

For comparison, the adsorption isotherm of BPA onto pure B@C powder was determined. Although B@C powder demonstrated adsorption capacity slightly higher (q_{max} = 112.43 mg/g) (Supplementary Material **SM12**), its incorporation into composite systems introduces practical trade-offs. Specifically, embedding B@C within the MFC matrix reduced the active material fraction from 100 % (neat powder) to 35.2 wt% and 12 wt% for MFC/8B@C and MFC/2B@C compositions, respectively. Despite this significant reduction in B@C content, the composite materials maintained exceptional adsorption performance while providing decisive operational advantages, such as moldable geometries, and simplified separation, that are absent in powder systems. One should notice that CTAB modified bentonite using other CTAB concentrations might lead to adsorbents with different adsorption capacity. For instance, when bentonite (20 g) was modified with CTAB at ~7×10^{-3} mol L^{-1}, the q_{max} reported for BPA was 15.22 mg/g [9].

To evaluate the practical applicability of the developed adsorbents, experiments were conducted using natural freshwater to assess performance under realistic environmental conditions (Figs. 7**E** and 7 **F**). The MFC/8B@C compositions demonstrated good performance towards the adsorption of BPA from freshwater, achieving q_{max} values of 69.89 mg/g (oven-dried) and 74.37 mg/g (freeze-dried). Interestingly, the oven-dried material exhibited enhanced performance in freshwater, increasing to 159 % of its capacity in MilliQ® water (69.89 vs 43.99 mg/g). This improvement possibly resulted from two synergistic mechanisms. First, salting-out effects from natural water salinity reduced BPA solubility and drove its partitioning toward the hydrophobic CTAB phase. Second, divalent cations improved CTAB packing density, increasing available binding sites [54]. Conversely, the cryogels in fresh water presented a reduction of 24 % of adsorption capacity in comparison to that in MilliQ® water (74.37 vs 98.51 mg/g). It is probably due to competing organic matter such as humic and fulvic acids commonly found in natural waters. Despite interference from these organic constituents through competitive binding, both MFC/8B@$C^{O.}$ and MFC/8B@$C^{F.D.}$ maintained substantial adsorption capacities, confirming their practical viability for real-world water treatment applications.

Processing methodology critically influenced adsorption efficiency. Freeze-drying consistently outperforms oven-drying across all compositions, with MFC/8B@C demonstrating the most pronounced improvement: q_{max} increase from 43.99 mg/g (oven) to 98.51 mg/g (freeze-dried) (Table 3), although elemental analysis indicated similar CTAB contents in MFC/8B@$C^{O.}$ (16.7 wt% CTAB) and MFC/8B@$C^{F.D.}$ (18.5 wt% CTAB). Therefore, this performance disparity reflects distinct structural architectures created by each drying method. Similar trends were observed for the adsorption of methylene blue on freeze-dried (545.6 mg/g) and air-dried (382.8 mg/g) alginate-based beads [28].

The BPA removal efficiency at 1.0 mL using MFC/2B@$C^{O.}$, MFC/8B@$C^{O.}$, MFC/2B@$C^{F.D.}$, and MFC/8B@$C^{F.D.}$ adsorbents amounted to 71 ± 11 %, 89.2 ± 0.6 %, 81 ± 1 %, and 55 ± 8 %, respectively (Supplementary Material **SM13**). The same trend was observed for the q_e values that ranged from 0.55 ± 0.08 mg/g to 0.90 ± 0.01 mg/g. The presence of competing cations showed no statistically significant effect on BPA removal (p = 0.991), with observed numerical variations falling within experimental variability. Statistical analysis confirmed no significant differences attributable to adsorbent type, drying method, bentonite content, or their interactions. The adsorbents demonstrated consistent performance under both pure BPA and mixed cation conditions, indicating applicability for real water treatment scenarios where BPA is present at low concentrations alongside competing ions.

To verify CTAB leaching from the composites during adsorption experiments, samples were immersed in MilliQ® water for 1 h at (22 ± 1) °C, and surface tension of the aqueous medium was measured. Results revealed that CTAB release correlated with initial loading: MFC/8B@CF.D. exhibited higher release (0.4 mmol/L, 48.28 mN/m) compared to MFC/2B@CF.D. (0.3 mmol/L, 52 mN/m) (Supplementary Material **SM14**), representing the leaching of weakly bound surfactant. Elemental analysis confirmed carbon associated with CTAB at 0.5 ± 0.1 % (5 ± 1 μg/L) for MFC/2B@$C^{F.D.}$ and 2.7 ± 0.2 % (27 ± 2 μg/L) for MFC/8B@$C^{F.D.}$; nitrogen remained below the detection limit. These residual CTAB concentrations are well below the IC_{50} range reported for marine species (554–1500 μg/L) [55], indicating minimal ecotoxicological risk and demonstrating environmental suitability of the treatment process. IC_{50} represents the concentration causing 50 % inhibition of a biological endpoint after defined exposure. Despite this leaching, MFC/8B@$C^{F.D.}$ demonstrates superior adsorption capacity (98.51 mg/g), indicating that initial CTAB loading was sufficiently high to retain adequate surface-bound surfactant even after desorption. This confirms that optimal modification requires initial surfactant excess to compensate for partial leaching and ensure sustained hydrophobic domain availability for BPA interaction.

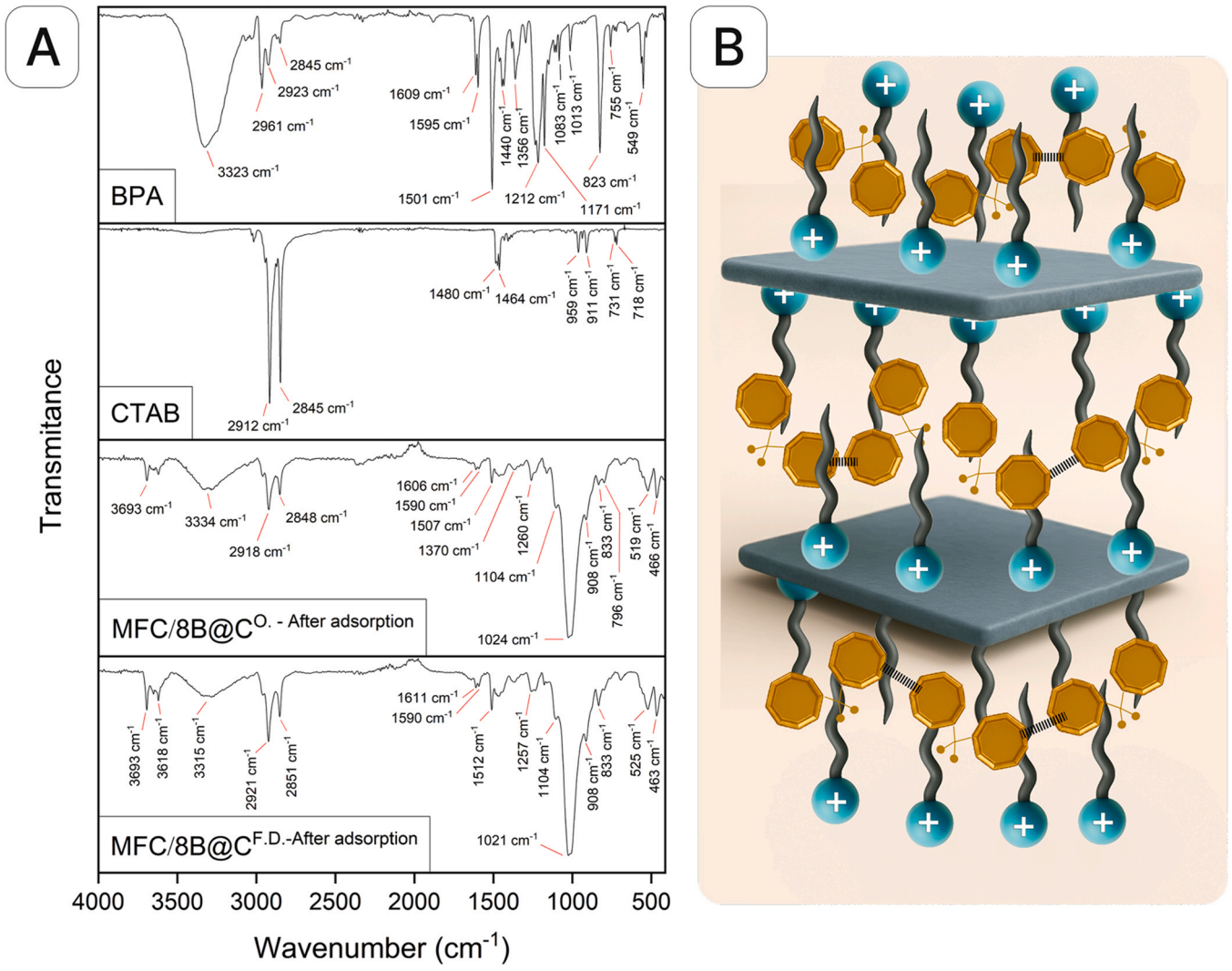

Fig. 8. (A) FTIR spectra of BPA, CTAB, MFC/8B@C$^{O.}$ and MFC/8B@C$^{F.D.}$ after BPA adsorption. (B) Schematic representation of BPA molecules adsorbed on the hydrophobic region provided by CTAB molecules, the dot lines represent possible π-π stacking between BPA aromatic rings.

Subsequently to the BPA adsorption experiments, MFC/8B@C$^{O.}$ and MFC/8B@C$^{F.D.}$ adsorbents were oven dried at 60 °C and analysed using FTIR-ATR. The FTIR spectra in Fig. 8**a** revealed the successful incorporation of BPA molecules. The characteristic aromatic C=C stretching vibrations of BPA were observed at 1606–1611 cm^{-1} and 1590 cm^{-1} [56,57], demonstrating effective adsorption onto both xerogel and cryogel structures. Furthermore, additional BPA-related bands were potentially observable in the adsorbent spectra: BPA's methyl stretching vibrations from the isopropylidene bridge ($\nu_{as}(CH_3)$ at ~2970 cm^{-1} and $\nu_s(CH_3)$ at ~2873 cm^{-1}) potentially overlap with CTAB's aliphatic region [56,57]. Spectral analysis revealed that the identified BPA bands at 1609 and 1595 cm^{-1} in the MFC/8B@C adsorbents exhibited minimal frequency shifts compared to pure BPA reference values (typically 1609 and 1590 cm^{-1}). The intense band at 823 cm^{-1} was assigned to the out-of-plane aromatic C–H bending vibration observed for pure BPA. After adsorption of BPA on MFC/8B@C adsorbents this band shifted to 833 cm^{-1} . These weak shifts suggest predominantly physical adsorption mechanisms, where BPA molecules interact with the composite matrix through weak intermolecular forces rather than strong chemical bonding. The spectroscopic evidence collectively indicates a dual-mode adsorption mechanism where BPA molecules are stabilized through: (i) hydrophobic interactions with CTAB's alkyl chains, particularly when BPA remains in its neutral molecular form [7,13], (ii) interactions between BPA's aromatic rings and the electron-rich regions of the intercalated CTAB-bentonite system [12], and (iii) possible π-π stacking between BPA aromatic rings, as depicted in Fig. 8**B**.

3.2.3. *Fixed-bed column adsorption experiments*

Understanding adsorbate-substrate equilibrium interactions through batch adsorption studies is fundamental; nevertheless, column adsorption systems demonstrate greater suitability for high-volume wastewater treatment due to their capacity for operational optimization and enhanced efficiency. Although the BPA removal capacity of MFC/2B@C was lower than that of MFC/8B@C under equilibrium conditions (as shown in Supplementary Material **SM15**), column adsorption experiments were nevertheless conducted for both compositions to evaluate their performance under dynamic flow conditions, which can differ significantly from equilibrium behavior.

Figs. 9**a** and 9**b** show the breakthrough curves obtained through the fixed-bed column experiments for BPA solutions on MFC/2B@C$^{O.}$, MFC/2B@C$^{F.D.}$, and MFC/8B@C$^{O.}$, MFC/8B@C$^{F.D.}$ adsorbents, respectively. The mass of adsorbent initial m (600 mg) was fixed and the drying method (oven and freeze-drier) was varied. Experimental data were fitted using the nonlinear Thomas model to evaluate how the adsorbent amount (m), the initial concentration of the adsorbate (C_0), and the flow rate (ν) through the column influence the adsorption capacity (q_0) [58]:

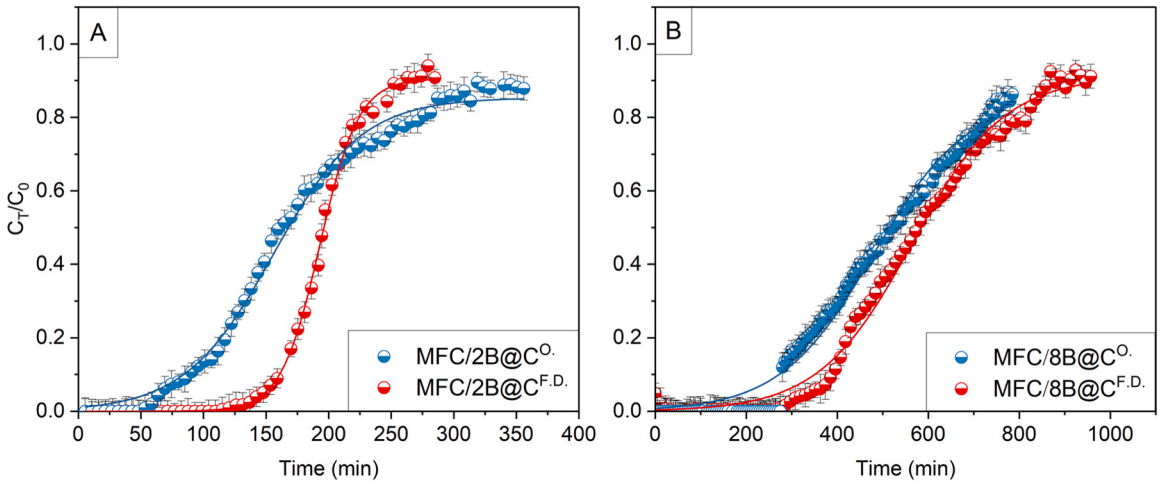

Fig. 9. Breakthrough curves obtained for BPA in distilled water (pH 6.12), using (A) MFC/2B@C$^{O.}$ and MFC/2B@C$^{F.D.}$, and (B) MFC/8B@C$^{O.}$, MFC/8B@C$^{F.D.}$ adsorbents. The experiments were conducted at $\nu = 0.4$ mL/min. The adsorbent mass and the initial concentration were set as 600 mg and at 291 and 276 mg/L, respectively. The solid lines are the non-linear fittings to Thomas model.

$$\frac{C_T}{C_0} = \frac{1}{1 + \exp\left[\frac{K_{Th}}{\nu} q_0 m - K_{Th} C_0 t\right]} \quad (2)$$

where C_T is the concentration of effluent at any time and the corresponding time (t), and K_{TH} is the Thomas rate constant (mL/min.mg). The Thomas model is ideal for predicting adsorption by disregarding internal and external diffusion resistances [58]. Data fitting was conducted using OriginPro 2024 software, employing a non-linear fitting method known as slogistic1, comparable to the Thomas model, as detailed in Supplementary Material **SM16**. Table 4 presents the experimental conditions for the breakthrough curves of BPA solutions on MFC/B@C, along with the non-linear fitting parameters of Thomas model, K_{TH} (L/mg.min) and theoretical maximal adsorption capacity q_0 (mg/g). The C_0 of BPA was set either as 276 mg/L or 291 mg/L. Column adsorption experiments were not performed using freshwater because after 8 h adsorption the C_T/C_0 values were less than 0.1, indicating the excessive experimental time required and the high adsorption capacity towards BPA dissolved in fresh water. On the other hand, the long saturation time indicated that the adsorbents efficiency remained for BPA in fresh water.

Table 4 demonstrates that the freeze-dried material (MFC/8B@C$^{F.D.}$) exhibited an adsorption capacity (q_0) of 115.92 mg/g, corresponding to a 9.3 % increase compared to the oven-dried material (MFC/8B@C$^{O.}$, q_0 = 105.08 mg/g). The rate constant (K_{TH}) remained similar for both MFC/8B@C$^{F.D.}$ and MFC/8B@C$^{O.}$, indicating that the drying process did not significantly alter the mass transfer mechanism. Unlike in batch experiments, under flow conditions, the transport of BPA molecules is governed not only by diffusion but also by convective forces, which drive the molecules to permeate through the entire porous network. This continuous flow likely reduces the influence of localized porosity variations created by different drying methods, thereby softening their impact on the overall adsorption kinetics.

The MFC/2B@C system exhibited substantially lower adsorption capacities due to reduced B@C content, achieving q_0 values of 36.29 mg/g (oven-dried) and 42.38 mg/g (freeze-dried). Breakthrough curves data show that MFC/8B@C systems (785–957 min) achieved 2.7-fold longer operational times than MFC/2B@C systems (284–356 min), evidencing that higher B@C content extends column lifespan regardless of drying method, confirming that preserved porous structure enhances mass transfer kinetics despite higher adsorption capacities.

Comparative analysis revealed exceptional performance of both developed materials against adsorbents reported in the literature. The magnitude of the increments established differences of significant order, ranging from 2.3-fold superior to KF/CTAB [12] up to exceptional values of two orders of magnitude superior to AAS [59], evidencing the distinctive efficacy of the developed system. The oven-dried material (q_0 = 105.08 mg/g) likewise surpassed all evaluated adsorbents, demonstrating the effectiveness of the MFC/8B@C system regardless of the applied drying method.

Microstructure plays a central role in determining adsorbate accessibility to adsorption sites. Oven-dried xerogels (MFC/2B@C$^{O.}$ and

Table 4
Experimental conditions applied for the breakthrough curves of BPA on MFC/B@C: C_0, v, and m_{ads} stand for inlet concentration (mg/L), flow rate (mL/min), mass of adsorbent (g), respectively. Fitting parameters of Thomas model K_{TH} (L/mg.min) and q_0 (mg/g) stand for the rate constant and adsorption capacity, respectively.

Pollutant/ Adsorbent	Experimental conditions				Fitting parameters of Thomas model			Ref
	C_0 (mg/L)	ν (mL/min)	Z (cm)	m_{ads} (mg)	K_{TH} (L/mg.min)	q_0 (mg/g)	R^2	
MFC/2B@C$^{O.}$	291	0.41	2	600	0.00044	36.29	0.9936	This work
MFC/2B@C$^{F.D.}$	291	0.41	2	600	0.00095	42.38	0.9986	
MFC/8B@C$^{O.}$	276	0.41	2	600	0.00015	105.08	0.986	
MFC/8B@C$^{F.D.}$	276	0.41	2	600	0.00003916	115.92	0.9936	
KF/CTAB	80	0.8	1.5	200	0.01517	35.24	0.9964	[12]
CMC/BG/CTAB	109	0.8	-	170	0.0011	31.69	0.9905	[13]
AHS	10	1	-	500	0.00395	2.035	0.999	[59]
AAS	10	1	-	500	0.00527	1.285	0.998	
A-m-MWCNTs	20	3	2	-	0.008	15.49	0.957	[60]

Legend: KF/CTAB: kapok fiber modified with CTAB; CMC/BG/CTAB: CTAB-modified carboxymethyl cellulose/bagasse cryogels; AHS: aluminum-HDTMA-sericite; AAS: aluminum-HDTMA-sericite; A-m-MWCNTs: Aliquat 336-impregnated magnetic multiwalled carbon nanotubes.

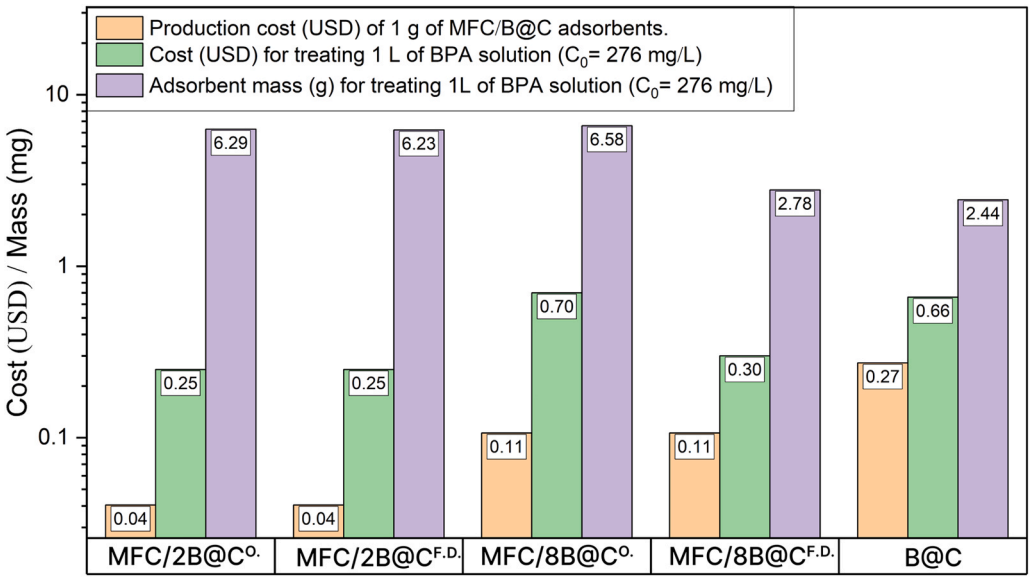

Fig. 10. Production cost (USD) of 1 g of B@C or MFC/B@C adsorbents, cost (USD) for BPA removal per liter of solution, and adsorbent mass required for BPA removal per liter of solution (g).

MFC/8B@C$^{O.}$) exhibited the lowest porosity and surface area due to structural collapse during drying, including cellulose hornification, whereas freeze-drying preserved the porous network in cryogels (MFC/2B@C$^{F.D.}$ and MFC/8B@C$^{F.D.}$) with significantly higher porosity and surface area. In batch adsorption, where agitation promotes contact but penetration through collapsed pores may be heterogeneous, MFC/8B@C$^{F.D.}$ achieved the highest capacity (98.51 mg/g) due to its greater CTAB content combined with high porosity facilitating site accessibility. Column operation, where constant flow ensures homogeneous solution penetration through the adsorbent bed, revealed substantial performance improvements: MFC/8B@C$^{O.}$ capacity increased from 41.61 to 105.08 mg/g, while MFC/8B@C$^{F.D.}$ rose modestly from 98.51 to 115.92 mg/g. Both MFC/8B@C$^{O.}$ xerogels (74.7 % porosity) and MFC/8B@C$^{F.D.}$ cryogels (93.7 % porosity) exhibited the highest column capacities, confirming that CTAB content and high porosity are critical factors governing performance.

4. Cost analysis

Fig. 10 shows the economic evaluation of adsorbent materials for BPA removal (276 mg/L) and illustrates the cost-performance relationships among the different adsorbents. For this purpose, the maxim adsorption capacity values obtained from batch experiments (q_{max}, Table 3) were used. Column adsorption experiments were not considered, as the use of B@C particles in the column proved unsuitable due to particle leaching.

For the cost-performance estimates, the local cost of electricity, time and energy consumed in oven- and freeze-drying, cost of raw material and reactants at lab scale were considered. B@C particles showed the highest treatment cost at $0.66/L, despite requiring a relatively low adsorbent mass (2.44 g/L), primarily due to their elevated production cost ($0.27/g). The most cost-effective treatment was achieved by MFC/2BC formulations, with both oven-dried and freeze-dried variants delivering identical operational costs of $0.25/L, representing a 62 % cost reduction compared to B@C particles. However, these formulations required higher adsorbent masses (6.29 g and 6.23 g for oven and freeze-dried, respectively), because of the lower adsorptive capacity but it was compensated by significantly lower production costs ($0.040/g). MFC/8B@C$^{F.D.}$ demonstrated intermediate performance with a treatment cost of $0.30/L (55 % reduction vs B@C) and moderate adsorbent mass requirement (2.78 g/L). Notably, MFC/8BC$^{O.}$ showed the poorest economic performance at $0.70/L, even higher than B@C particles, combined with the highest adsorbent mass requirement (6.58 g/L). These findings indicate that, under the experimental conditions of this study, the lowest B@C content (2B@C) provided superior economic efficiency, while freeze-drying offered advantages primarily for 8B@C formulations by reducing required adsorbent mass. The incorporation of B@C particles into MFC matrices with optimized composition (MFC/2B@C) delivered the most economically viable solution for BPA removal applications.

5. Conclusions

This work provides the first systematic comparison between cryogels and xerogels of the MFC/B@C system for BPA removal in both batch and column adsorption studies. Recent literature on CTAB-modified biopolymers and clay-cellulose composites for organic pollutant removal presents critical limitations: exclusive batch adsorption evaluation without fixed-bed column validation, absence of comparative drying method analysis despite advanced porosity characterization, insufficient testing in real water matrices, and lack of comprehensive cost-benefit optimization balancing adsorption capacity and CTAB content. This work systematically addresses these gaps.

The MFC/B@C composites demonstrated outstanding performance in natural water matrices for the removal of BPA in the concentration range from 1.0 mg/L to 276 mg/L, despite interference effects from natural organic matter or competing ions, thereby establishing practical applicability limits that were not addressed in previous BPA removal studies. The fixed-bed column validation indicated that the B@C content played a more decisive role than porosity induced by the drying method, as the adsorption capacities of MFC/8B@C$^{O.}$ and MFC/8B@C$^{F.D.}$ reached 105.08 mg/g and 115.92 mg/g, respectively, which is approximately threefold higher than those of MFC/2B@C$^{O.}$ and MFC/2B@C$^{F.D.}$. Nevertheless, considering local operational costs and efficiency, the economic analysis performed for the BPA concentration range of 20 m/L to 276 mg/L indicated that MFC/2B@C represents the most suitable adsorbent for large-scale applications, irrespective of the drying method. Future work will extend this cost/efficiency analysis to the

environmentally relevant dilute range (< 0.1 mg/L).

CRediT authorship contribution statement

Denise F.S. Petri: Writing – review & editing, Visualization, Resources, Project administration, Funding acquisition, Conceptualization. **Mário A.B.S. Nunes:** Writing – original draft, Validation, Software, Methodology, Investigation, Formal analysis, Data curation. **Orlando J. Rojas:** Writing – review & editing, Visualization, Supervision, Resources, Conceptualization.

Declaration of Competing Interest

The authors declare that they have no known competing financial interests or personal relationships that could have appeared to influence the work reported in this paper.

Acknowledgements

This work was supported by the Conselho Nacional de Desenvolvimento Científico e Tecnológico (CNPq Grant 304017/2021–3) and São Paulo Research Foundation (FAPESP grants 2021/07305–8, 2023/14664–0, 2024/20008–0). The present work was carried out with the support of the Institute of Chemistry and its Analytical Center – Code CAIQUSP/100 and of the Bioproducts Institute (UBC, Vancouver). O.J. R. and M.A.B.S.N. also acknowledge the Canada Excellence Research Chair Program (Grant No. CERC-2018-00006).

Appendix A. Supporting information

Supplementary data associated with this article can be found in the online version at doi:10.1016/j.colsurfa.2026.139499.

Data availability

Data will be made available on request.

References

[1] J. Corrales, L.A. Kristofco, W.B. Steele, B.S. Yates, C.S. Breed, E.S. Williams, B. W. Brooks, Global assessment of bisphenol A in the environment: review and analysis of its occurrence and bioaccumulation, Dose-Response 13 (2015) 1559325815598308, https://doi.org/10.1177/1559325815598308.

[2] M.F. Manzoor, T. Tariq, B. Fatima, A. Sahar, F. Tariq, S. Munir, S. Khan, M.M. A. Nawaz Ranjha, A. Sameen, X.-A. Zeng, An insight into bisphenol A, food exposure and its adverse effects on health: a review, Front. Nutr. 9 (2022) 1047827, https://doi.org/10.3389/fnut.2022.1047827.

[3] O.T. Ologundudu, T.A.M. Msagati, O.E. Popoola, J.N. Edokpayi, Bisphenol A in selected south african water sources: a critical review, ACS Omega 10 (2025) 6279–6293, https://doi.org/10.1021/acsomega.4c01686.

[4] J.O. Ighalo, S.B. Kurniawan, B. Khongthaw, J. Buhari, P.K. Chauhan, J. Georgin, D. S.P. Franco, Bisphenol A (BPA) toxicity assessment and insights into current remediation strategies, RSC Adv. 14 (2024) 35128–35162, https://doi.org/10.1039/D4RA05628K.

[5] H. Abu Hasan, M.H. Muhamad, S. Budi Kurniawan, J. Buhari, O. Husain Abuzeyad, Managing bisphenol A contamination: advances in removal technologies and future prospects, Water 15 (2023) 3573, https://doi.org/10.3390/w15203573.

[6] C.B. Godiya, B.J. Park, Removal of bisphenol A from wastewater by physical, chemical and biological remediation techniques. A review, Environ. Chem. Lett. 20 (2022) 1801–1837, https://doi.org/10.1007/s10311-021-01378-6.

[7] Y. Gong, G. Liu, Q. Wang, A. Zhu, P. Liu, Q. Wu, Synthesis of a novel mesoporous Fe_3O_4@SiO_2/CTAB-SiO_2 composite material and its application in the efficient removal of bisphenol A from water, Colloid Polym. Sci. 299 (2021) 807–822, https://doi.org/10.1007/s11051-024-06202-0.

[8] Q. Zhou, X. Luo, J. He, J. Guo, C. Xu, Y. Wan, G. Xiong, Q. Xu, Bisphenol A and 17α-ethinylestradiol removal from water by hydrophobic modified acicular mullite, Sustainability 14 (2022) 14248, https://doi.org/10.3390/su142114248.

[9] N. Hadoudi, M. Ahari, N. Zaki, A. Charki, H. El Ouarghi, A. Bayoussef, M. Mansori, M. Fouad, A. Salhi, H. Amhamdi, Removal Efficiency of Phenolic Compounds (Bisphenol A and Pentachlorophenol) by Adsorption Using a Bentonite-CTAB, (2024). https://doi.org/10.5772/intechopen.1004783.

[10] I. Garikoé, B. Sorgho, A. Yaméogo, B. Guel, D. Andala, Removal of bisphenol A by adsorption on organically modified clays from Burkina Faso, Bioremediat. J. 25 (2020) 22–47, https://doi.org/10.1080/10889868.2020.1842321.

[11] S. Rovani, J.J. Santos, S.N. Guilhen, P. Corio, D.A. Fungaro, Fast, efficient and clean adsorption of bisphenol-A using renewable mesoporous silica nanoparticles from sugarcane waste ash, RSC Adv. 10 (2020) 27706–27712, https://doi.org/10.1039/D0RA05198E.

[12] M.A.B.S. Nunes, A.C.D.V. Boas, R. Fernandes, R. Itri, L.R. Marques, R.A. Ando, D.F. S. Petri, Kapok fibers modified with cationic surfactants: structural insights and efficient removal of Cr (VI) and bisphenol A, J. Colloid Interface Sci. 683 (2025) 1119–1134, https://doi.org/10.1016/j.jcis.2024.12.136.

[13] I.P. Meneses, S.D. Novaes, R.S. Dezotti, P.V. Oliveira, D.F.S. Petri, CTAB-modified carboxymethyl cellulose/bagasse cryogels for the efficient removal of bisphenol A, methylene blue and Cr (VI) ions: batch and column adsorption studies, J. Hazard. Mater. 421 (2022) 126804, https://doi.org/10.1016/j.jhazmat.2021.126804.

[14] A.A.B. Omran, A.A.B.A. Mohammed, S.M. Sapuan, R.A. Ilyas, M.R.M. Asyraf, S. S. Rahimian Koloor, M. Petrů, Micro-and nanocellulose in polymer composite materials: a review, Polymers 13 (2021) 231, https://doi.org/10.3390/polym13020231.

[15] D. Ewis, M.M. Ba-Abbad, A. Benamor, M.H. El-Naas, Adsorption of organic water pollutants by clays and clay minerals composites: a comprehensive review, Appl. Clay Sci. 229 (2022) 106686, https://doi.org/10.1016/j.clay.2022.106686.

[16] N. Job, A. Théry, R. Pirard, J. Marien, L. Kocon, J.-N. Rouzaud, F. Béguin, J.-P. Pirard, Carbon aerogels, cryogels and xerogels: influence of the drying method on the textural properties of porous carbon materials, Carbon 43 (2005) 2481–2494, https://doi.org/10.1016/j.carbon.2005.04.031.

[17] N. Buchtová, T. Budtova, Cellulose aero-, cryo-and xerogels: towards understanding of morphology control, Cellulose 23 (2016) 2585–2595, https://doi.org/10.1007/s10570-016-0960-8.

[18] N. Dai, X. Liu, L. Yang, X. Huang, D. Song, S. Wang, K. Zhang, X. Liu, W. Dong, Y. Zhang, Cetyltrimethylammonium bromide-modified laponite@diatomite composites for enhanced adsorption performance of organic pollutants, Langmuir 40 (2024) 8427–8439, https://doi.org/10.1021/acs.langmuir.3c03938.

[19] J. Ouyang, X. Zhang, X. Qi, C. Wang, Y. Yuan, X. Xie, J. Qiao, X. Guo, Y. Wu, Enhanced sorption and fluorescent detection of bisphenol A by using sodium alginate/cellulose nanofibrils/ZIF-8 composite hydrogel, Int. J. Biol. Macromol. 271 (2024) 132198, https://doi.org/10.1016/j.ijbiomac.2024.132198.

[20] J. Abdi, G. Mazloom, Y. Yoon, Surface modification of MXene using cationic CTAB surfactant for adsorptive elimination of cefazolin antibiotic from water, Sci. Rep. 15 (2025) 16416, https://doi.org/10.1038/s41598-025-01435-y.

[21] H. Du, Z. Wang, K.J. Shah, Y. Sun, Preparation of CTAB-ATP/CTS composite adsorbent and removal performance of Norfloxacin in water, Water 16 (2024) 2446, https://doi.org/10.3390/w16172446.

[22] C. Ma, L. Yi, J. Yang, J. Tao, J. Li, Nanocellulose–organic montmorillonite nanocomposite adsorbent for diuron removal from aqueous solution: optimization using response surface methodology, RSC Adv. 10 (2020) 30734–30745, https://doi.org/10.1039/D0RA04853D.

[23] Y. Zhu, Y. Cui, Y. Peng, R. Dai, H. Chen, Y. Wang, Preparation of CTAB intercalated bentonite for ultrafast adsorption of anionic dyes and mechanism study, Colloids Surf. A Physicochem. Eng. Asp. 658 (2023) 130705, https://doi.org/10.1016/j.colsurfa.2022.130705.

[24] N. My Linh, L. Duong, T. Van Duc, H. Thi Anh Thu, N. Khac Lieu, P. Van Hung, N. Hoa, L.T. Quang Khieu, D. Phenol red adsorption from aqueous solution on the modified bentonite, J. Chem. 2020 (2020) 1504805, https://doi.org/10.1155/2020/1504805.

[25] A. Mokhtar, F. Bennabi, S. Abdelkrim, A. Sardi, B. Boukoussa, A. Souna, A. Bengueddach, M. Sassi, Evaluation of intercalated layered materials as an antimicrobial and drug delivery system: a comparative study, J. Incl. Phenom. Macrocycl. Chem. 96 (2020) 353–364, https://doi.org/10.1007/s10847-020-00978-z.

[26] M.R. Caruso, M.M. Calvino, P. Šiler, L. Cába, S. Milioto, L. Lisuzzo, G. Lazzara, G. Cavallaro, Self-standing biohybrid xerogels incorporating nanotubular clays for sustainable removal of pollutants, Small 21 (2025) 2405215, https://doi.org/10.1002/smll.202405215.

[27] N. Buchtová, C. Pradille, J.-L. Bouvard, T. Budtova, Mechanical properties of cellulose aerogels and cryogels, Soft Matter 15 (2019) 7901–7908, https://doi.org/10.1039/C9SM01028A.

[28] S. Kondaveeti, D.F.S. Petri, H.E. Jeong, Efficiency of air-dried and freeze-dried alginate/xanthan beads in batch, recirculating and column adsorption processes, Int. J. Biol. Macromol. 204 (2022) 345–355, https://doi.org/10.1016/j.ijbiomac.2022.02.011.

[29] M.V. Dumitru, T. Sandu, A. Miron, A. Zaharia, I.C. Radu, A.-M. Gavrilă, A. Sârbu, H. Iovu, A.-L. Chiriac, T.V. Iordache, Hybrid cryogels with superabsorbent properties as promising materials for Penicillin G retention, Gels 9 (2023) 443, https://doi.org/10.3390/gels9060443.

[30] S. Longo, M. Mauro, C. Daniel, M. Galimberti, G. Guerra, Clay exfoliation and polymer/clay aerogels by supercritical carbon dioxide, Front. Chem. 1 (2013) 28, https://doi.org/10.3389/fchem.2013.00028.

[31] B.C. Moggio, R. Bergamasco, C.M.G. Andrade, L.B.R. Aylon, On the analysis of cryogels and xerogels using cellulose nanofibers and graphene oxide, Polymers 15 (2023) 3833, https://doi.org/10.3390/polym15183833.

[32] Y. Dong, H. Li, Y. Fan, X. Ma, D. Sun, Y. Wang, Z. Gao, X. Dong, Tunable dewatering behavior of montmorillonite suspension by adjusting solution pH and electrolyte concentration, Minerals 10 (2020) 293, https://doi.org/10.3390/min10040293.

[33] K.J. Shah, M.K. Mishra, A.D. Shukla, T. Imae, D.O. Shah, Controlling wettability and hydrophobicity of organoclays modified with quaternary ammonium surfactants, J. Colloid Interface Sci. 407 (2013) 493–499, https://doi.org/10.1016/j.jcis.2013.05.050.

[34] K. Li, Z. Zeng, J. Xiong, L. Yan, H. Guo, S. Liu, Y. Dai, T. Chen, Fabrication of mesoporous Fe_3O_4@SiO_2@CTAB–SiO_2 magnetic microspheres with a core/shell structure and their efficient adsorption performance for the removal of trace PFOS from water, Colloids Surf. A Physicochem. Eng. Asp. 465 (2015) 113–123, https://doi.org/10.1016/j.colsurfa.2014.10.044.
[35] W.-T. Tsai, C.-W. Lai, T.-Y. Su, Adsorption of bisphenol-A from aqueous solution onto minerals and carbon adsorbents, J. Hazard. Mater. 134 (2006) 169–175, https://doi.org/10.1016/j.jhazmat.2005.10.055.
[36] M. Wohlert, T. Benselfelt, L. Wågberg, I. Furó, L.A. Berglund, J. Wohlert, Cellulose and the role of hydrogen bonds: not in charge of everything, Cellulose 29 (2022) 1–23, https://doi.org/10.1007/s10570-021-04325-4.
[37] M.E. Parolo, G.R. Pettinari, T.B. Musso, M.P. Sánchez-Izquierdo, L.G. Fernández, Characterization of organo-modified bentonite sorbents: the effect of modification conditions on adsorption performance, Appl. Surf. Sci. 320 (2014) 356–363, https://doi.org/10.1016/j.apsusc.2014.09.105.
[38] A. Suratman, A.Z. Adhyana, D. Siswanta, The effect of CTAB on bentonite for slow release fertilizer, Key Eng. Mater. 884 (2021) 226–233, https://doi.org/10.4028/www.scientific.net/KEM.884.226.
[39] B. Zohra, K. Aicha, S. Fatima, B. Nourredine, D. Zoubir, Adsorption of Direct Red 2 on bentonite modified by cetyltrimethylammonium bromide, Chem. Eng. J. 136 (2008) 295–305, https://doi.org/10.1016/j.cej.2007.03.086.
[40] C.-Y. Cao, L.-K. Meng, Y.-H. Zhao, Adsorption of phenol from wastewater by organo-bentonite, Desalin. Water Treat. 52 (2014) 3504–3509, https://doi.org/10.3390/separations10100523.
[41] Y. Chen, Y. Jiang, J. Wan, Q. Wu, Z. Wei, Y. Ma, Effects of wet-pressing induced fiber hornification on hydrogen bonds of cellulose and on properties of eucalyptus paper sheets, Holzforschung 72 (2018) 829–837, https://doi.org/10.1515/hf-2017-0214.
[42] N.A.A. Anas, Y.W. Fen, N.A. Yusof, N.A.S. Omar, N.S.M. Ramdzan, W.M.E.M. M. Daniyal, Investigating the properties of cetyltrimethylammonium bromide/hydroxylated graphene quantum dots thin film for potential optical detection of heavy metal ions, Materials 13 (2020) 2591, https://doi.org/10.3390/ma13112591.
[43] J.M. Gisbert-González, V. Briega-Martos, F.J. Vidal-Iglesias, Á. Cuesta, J.M. Feliu, E. Herrero, Spectroelectrochemical studies of CTAB adsorbed on gold surfaces in perchloric acid, Langmuir 39 (2023) 2761–2770, https://doi.org/10.1021/acs.langmuir.2c03226.
[44] A.M. Gerakis, M.A. Koupparis, Physicochemical studies of the cetyltrimethylammonium bromide micellar system using a bromide selective electrode, Talanta 41 (1994) 765–773.
[45] O.R. Kam, I. Garikoe, C. Bakouan, B. Guel, Low-cost synthesis of alumina nanoparticles and their usage for Bisphenol-A removal from aqueous solutions, Processes 9 (2021) 1709, https://doi.org/10.3390/pr9101709.
[46] Y. Zhang, C. Liu, L. Luo, Y. Shi, Y. Chen, S. Wang, L. Bian, F. Jiang, One-step hydrothermal synthesis of CTAB-modified SiO_2 for removal of bisphenol A, Water Sci. Technol. 76 (2017) 928–938, https://doi.org/10.2166/wst.2017.272.
[47] Y.-S. Ho, G. McKay, Pseudo-second order model for sorption processes, Process Biochem. 34 (1999) 451–465, https://doi.org/10.1016/S0032-9592(98)00112-5.
[48] E. Dovi, A.A. Aryee, A.N. Kani, F.M. Mpatani, J. Li, Z. Li, L. Qu, R. Han, Fixed-bed Adsorption of Congo red dye and Bisphenol A from solution onto surfactant modified walnut shell, (2021). https://doi.org/10.1007/s11356-021-12550-4.
[49] C. Jiménez-Saelices, B. Seantier, B. Cathala, Y. Grohens, Spray freeze-dried nanofibrillated cellulose aerogels with thermal superinsulating properties, Carbohydr. Polym. 157 (2017) 105–113, https://doi.org/10.1016/j.carbpol.2016.09.068.
[50] I. Langmuir, The constitution and fundamental properties of solids and liquids. Part I. Solids, J. Am. Chem. Soc. 38 (1916) 2221–2295, https://doi.org/10.1021/ja02268a002.
[51] H. Freundlich, Über die adsorption in lösungen, Z. F. üR. Phys. Chem. 57 (1907) 385–470, https://doi.org/10.1515/zpch-1907-5723.
[52] O. Redlich, D.L. Peterson, A useful adsorption isotherm, J. Phys. Chem. 63 (1959) 1024, https://doi.org/10.1021/j150576a611.
[53] M.J. Temkin, V. Pyzhev, 1940, Recent Modifications to Langmuir Isotherms.
[54] Z.-M. Wang, H. Ooga, T. Hirotsu, W.-L. Wang, Q.Y. Wu, H.-Y. Hu, Matrix-enhanced adsorption removal of trace BPA by controlling the interlayer hydrophobic environment of montmorillonite, Appl. Clay Sci. 104 (2015) 81–87, https://doi.org/10.1016/j.clay.2014.11.011.
[55] O. Kaczerewska, R. Martins, J. Figueiredo, S. Loureiro, J. Tedim, Environmental behaviour and ecotoxicity of cationic surfactants towards marine organisms, J. Hazard. Mater. 392 (2020) 122299, https://doi.org/10.1016/j.jhazmat.2020.122299.
[56] R. Ullah, I. Ahmad, Y. Zheng, Fourier transform infrared spectroscopy of "bisphenol A", J. Spectrosc. 2016 (2016) 2073613, https://doi.org/10.1155/2016/2073613.
[57] R. Ullah, X. Wang, Molecular vibrations of bisphenol "S" revealed by FTIR spectroscopy and their correlation with bisphenol "A" disclosed by principal component analysis, Appl. Opt. 57 (2018) D20–D26, https://doi.org/10.1364/AO.57.000D20.
[58] H.C. Thomas, Heterogeneous ion exchange in a flowing system, J. Am. Chem. Soc. 66 (1944) 1664–1666, https://doi.org/10.1021/ja01238a017.
[59] S.M. Lee, D. Tiwari, Use of hybrid materials in the decontamination of bisphenol A from aqueous solutions, RSC Adv. 4 (2014) 43921–43930, https://doi.org/10.1039/c4ra06793b.
[60] D. Bhatia, D. Datta, Removal of bisphenol-A using amine-modified magnetic multiwalled carbon nanotubes: batch and column studies, J. Chem. Eng. Data 64 (2019) 2877–2887, https://doi.org/10.1021/acs.jced.9b00240.